Surfactant- and template-free hydrothermal assembly of Cu2O visible light photocatalysts for trimethoprim degradation

Surfactant- and template-free hydrothermal assembly of Cu_2O visible light photocatalysts for trimethoprim degradation

Sekar Karthikeyan,[a] Chitiphon Chuaicham,[a] Umamahesh Balijapalli,[b] Wei Li,[c] Karen Wilson,[d] Adam F. Lee,[d]* Keiko Sasaki,[a]*

[a]*Department of Earth Resources Engineering, Faculty of Engineering, Kyushu University, 744 Motooka, Nishiku, Fukuoka 819-0395, Japan*

[b]*Center for Organic Photonics and Electronics Research (OPERA), Kyushu University, 744 Motooka, Nishiku, Fukuoka 819-0395, Japan*

[c]*European Bioenergy Research Institute, Aston University, Birmingham B4 7ET, UK*

[d]*Centre for Advanced Materials & Industrial Chemistry (CAMIC), School of Science, RMIT University, Melbourne VIC 3000, Australia.*

*Corresponding Authors: E-mail: keikos@mine.kyushu-u.ac.jp , Tel: +81-92-802-3338; adam.lee2@rmit.edu.au

Abstract

A surfactant-free, low temperature hydrothermal synthesis of Cu_2O nanostructures is demonstrated for application to the photocatalytic degradation of trimethoprim (TMP), an environmental xenobiotic. Photophysical properties of different size and shape Cu_2O nanostructures were determined by bulk and surface microscopic and spectroscopic analyses. Visible light photoactivity for the oxidative degradation of TMP is sensitive to the rate of photoexcited charge carrier bulk recombination, and therefore the size of Cu_2O crystallites. Optimum photodegradation activity was observed for a hierarchical Cu_2O nanostructure, comprising 11 nm crystallites nucleated as 50-80 nm particles, themselves coalesced into 400 nm compact agglomerates. The specific activity of 1.12 $\mu mol.g^{-1}.min^{-1}$ for a 0.1 mM TMP aqueous solution is comparable to previous reports that required higher energy and/intensity UV irradiation. The stepwise hydroxylation and oxidative cleavage of TMP to form monocylic fragments is driven by hydroxyl radicals photogenerated over the hierarchical Cu_2O nanostructure, which exhibits excellent catalytic stability for >25 h.

Keywords: *Photocatalysis, hierarchical, copper, trimethoprim, xenobiotic*

1. Introduction

Nanostructured catalysts are in high demand for diverse industrial applications due to their unique electronic and geometric properties which may confer high activity, selectivity and lifetime. Assembly of catalytic nanoparticles into hierarchical structures can improve mechanical stability and active surface area, and tune their photophysical properties such as light harnessing capacility, for enhanced thermal and photocatalysis

[1-5]. Many hierarchical photocatalysts mimic natural structures such as flower- [6], tree- [7], brush- [8] and urchin-like[9] materials, but their preparation and scale-up is often hindered by the requirement for expensive/hazardous reagents and/or significant costs and time associated with multi-step syntheses employing hard templates, surfactants (e.g. cetyl ammonium bromide and sodium dodecyl sulfate) or other structure directing agents (e.g. polyethylene glycol, polyvinyl pyrrolidine or amino acids) and high temperatures. New atom- and energy efficient synthetic strategies to hierarchical photocatalysts, incorporating Earth abundant elements, are therefore highly desirable.

Copper oxide (Cu_2O) is a low cost p-type semiconductor with a visible light band gap of ~2.0–2.2 eV [10-12] and unique photophysical properties including a high absorption coefficient and conductivity, and excellent photocatalytic activity for solar fuels production and environmental remediation [13, 14]. We recently demonstrated a one- pot, hydrothermal route to hierarchical Cu_2O nanospheres for photocatalytic H_2 production and 4-chlorophenol decomposition [15].

Although Cu_2O has excellent visible light harnessing properties[16], it suffers from poor photostability and modest activity. Syntheses often employ surfactants, such as polyvinylpyrrolidone (PVP) [17], sodium dodecyl sulfate (SDS) [18-21] or polyethylene glycol (PEG) [22] which in some cases confer size control (e.g. 40 to 420 nm nanocubes using SDS [23]), high temperatures (e.g. 360 °C in air for mixed oxidation state nanocube photocatalysts [24] or 200 °C for hierarchical hollow CuO/Cu_2O microspheres [25]), toxic chemicals such as 1-hexadecylamine [26], and/or complex multistep routes as for Si(100) templated core–shell $Cu–Cu_2O$ shape controlled nanoparticles [27], Cu_2O/CuO bilayered composites using electrochemical and hydrothermal processes [28], and $Cu/Cu_2O/CuO$ composites (using earth-scarce and toxic components at 500 °C [29]). The use of surfactants or polymer stabilizers is problematic since long chain surfactants/stabilisers can block access to surface active sites thereby poisoning reactivity [30] or on occasion promote reactivity [31]. In any event, the influence of bulky stabilisers on catalysis is hard to predict, and their removal from nanoparticle surfaces is difficult and can induce undesired particle agglomeration and a concomitant loss of active surface area.

We previously reported [32] the preparation of well-defined Cu_2O nanocube photocatalysts with sizes from 50 to 500 nm using PEG as a structure-directing agent. These nanocube photocatalysts exhibited enhanced water splitting but suffered from relatively poor stability. Cupric oxide (CuO) is an n-type semiconductor with a band gap range of 1.2–1.7 eV, and an excellent co-catalyst [33] for Cu_2O that improves charge separation, thereby suppressing recombination of photogenerated electron-hole pairs at the CuO/Cu_2O interface [34, 35]. Hollow, hierarchical, core-shell $CuO@Cu_2O$, Cu_2O, and $Cu/CuO@Cu_2O$ nanostructures also exhibit improved Cu_2O photostability [22]. Continuing fundamental interest in structure-function relationships for semiconductor photocatalysts, and a desire for greener routes to their synthesis, underpin the current study of a new and simple route to the assembly of hierarchical CuO/Cu_2O and Cu/Cu_2O nanostructures.

Trimethoprin (TMP) is an emerging and stable antibiotic used worldwide for human and veterinary medicine [36]. A recent survey found unacceptable TMP concentrations from ng/L to μg/L in 37 Japanese rivers, with the highest levels (up to 6999 ng/L) in Tokyo municipal wastewater and livestock wastewater [37]. Environmental monitoring has also identified μg/L quantities of TMP in effluent treatment plants [38]. In the United States, TMP levels in wastewater range from 0.011 to 0.53 μg L^{-1}, with existing technologies able to remove <10 % of this [39]. The presence of such xenobiotics in aquatic ecosystems is undesirable since it promotes the emergence of resistant bacteria [40], and low cost technologies to eliminate TMP from contaminated water streams are therefore sought.

Here we report a one-pot, surfactant-free, mild (60 °C) hydrothermal route to hierarchical cubic and nanostructured Cu_2O photocatalysts of controllable sizes (400 nm to 2.5 μm) for TMP removal. Hierarchical Cu_2O nanoparticles were applied to the photocatalytic oxidative degradation of trimethoprim, with the resulting degradation activity under visible light comparable to that previously reported under high energy and/or intensity UV light [41]. This synthetic methodology offers a new atom and energy efficient route to hierarchical nanostructured thermal and photocatalysts for applications in environmental remediation solar fuels, and the production of high value chemicals.

2. Experimental

2.1. Chemicals

The following chemicals were used as received: copper(II) acetate monohydrate ($Cu(C_2H_3O_2)_2 \cdot H_2O$, 98%; Wako), copper(II) sulfate pentahydrate ($CuSO_4 \cdot 5H_2O$, 98%; Wako), copper(II) chloride dihydrate ($CuCl_2 \cdot 2H_2O$, 99%; Wako), ascorbic acid ($C_6H_8O_6$, 99.6%; Wako), hydrazine monohydrate ($H_4N_2 \cdot H_2O$, 98%; Wako), hydroxylammonium chloride ($NH_2OH \cdot HCl$; Sigma-Aldrich; 98%), sodium hydroxide (NaOH, 98%; Wako), ethanol (C_2H_5OH, 99.5%; Wako), trimethoprim ($C_{14}H_{18}N_4O_3$, 98%; TCI, Japan), acetonitrile (C_2H_3N, 99.8%; Wako), high-performance liquid chromatography (HPLC) water (Wako, Japan), and formic acid (HCOOH, 98%; TCI, Japan).

2.2. Characterisation

Photophysical properties of the four catalysts were characterized by bulk and surface analytical methods. Powder X-ray diffraction (PXRD) was performed using a Rigaku Ultima IV diffractometer with Cu K_α radiation at 40 kV/40 mA with a step size of 0.02°. Band gaps (Eg) were calculated by diffuse reflectance UV-Vis spectroscopy (DRUVS) on a Shimadzu UV-2450 spectrophotometer equipped with an ISR-2200 integrating sphere. Solid state photoluminescence spectroscopy (PL) was performed using a JASCO F-6600 spectrofluorometer. High Resolution Transmission electron microscopy (HRTEM) imaging was conducted using a JEOL JEM-2100HCKM instrument, and field emission scanning electron microscopy (FE-SEM) imaging on a ZEISS ULTRA™ 55 instrument. HRTEM samples were prepared by dispersion in ethanol, sonication, drop casting on carbon coated copper grids (molybdenum grids were used for EDX elemental

mapping using a JED-2300T detector) and drying. X-ray photoelectron spectra (XPS) were collected on an ULVAC-PHI ESCA 5800 spectrometer using a monochromated Al K_α X-ray source operated at 200 W. Energy referencing was performed using the C 1s peak for adventitious carbon set to 284.6 eV, and peak fitting was undertaken using Casa XPS Version 2.3.16. Specific surface area and pore size analysis was performed using a BEL-Max N_2 porosimeter on degassed samples. LCMS analysis on an Agilent 6545 LC/Q-TOF using a ZORBAX SB-C100. Cu K-edge XANES spectra of the as-prepared catalysts and Cu foil, Cu_2O and CuO reference materials were measured on BL15 of the Kyushu Synchrotron Light Research Center (SAGA-LS; Tosu, Japan) in transmission mode. Samples were prepared by dilution with BN and mounted with Kapton tape. The photon energy was scanned using a Si double crystal monochromator from 8.9 to 9.2 keV. The storage ring operating current was 306.1 mA at 1.40 GeV. Linear combination fitting (LCF) analysis was performed using the Athena-Demeter 0.9.26 program in the IFEFFIT software package. Band gaps were determined from Tauc plots (**Fig. S1)** according to **Eqs. 1** and **2** assuming Cu_2O as the dominant phase and a direct band gap semiconductor.

$$\alpha h\nu = A(h\nu - E_g)^{\eta} \qquad \textbf{Eq. 1}$$

where, A is absorption coefficient, α is linear absorption coefficient, h -Planck's constant, $h\nu$ - photon energy and Eg band gap. The band gap was determined using the Kubelka-Munk formalism shown in **Eq. 2**:

$$a = \frac{(1-R)^2}{2R} \qquad \textbf{Eq. 2}$$

2.3. Synthesis of Cu_2O photocatalysts

Shape-controlled Cu_2O photocatalysts were synthesized by a simple, surfactant-free, low temperature route. Typically, 10 mL of 0.1 M copper acetate monohydrate ($Cu(C_2H_3O_2)_2{\cdot}H_2O$) was placed in a beaker and stirred at 450 rpm for 5 min in a 60 °C water bath. In a separate vessel, 0.1 M NaOH was added to the preceding copper acetate solution, and stirring continued for 7 min followed by dropwise addition of 1 mL of 0.1 M ascorbic acid to the copper–sodium hydroxide mixture until a brownish-yellow Cu_2O precipitate was formed. The reaction mixture was immediately sonicated for 2 min and then transferred to a vacuum filtration unit and washed three times with deionized water and then twice with ethanol. The filtrate was freeze dried for 24 h and the resulting solid, termed Cu_2O-B, was stored in a desiccator. The initial Cu(II) ions were precipitated as copper hydroxide by NaOH and then partially reduced to a Cu(I)/Cu(II) oxide by ascorbic acid. Since the choice of Cu precursor and reductant likely play an important role in controlling the density of Cu ions and Cu_2O composition and morphology, both reductant and Cu precursor were subsequently varied to produce a family of nanostructured materials. Cu_2O-A was synthesized using 1 mL of 0.1 M $N_2H_4{\cdot}H_2O$ as a reductant; Cu_2O-C using 10 mL of 0.1 M $CuSO_4{\cdot}5H_2O$ as a precursor; Cu_2O-D using

1 mL of 0.1 M $NH_2OH{\cdot}HCl$ as a reductant; Cu_2O-E using 10 mL of 0.1 M $CuSO_4{\cdot}5H_2O$ and 1 mL of 0.1 M $NH_2OH{\cdot}HCl$; and finally Cu/Cu_2O-F using 10 mL of a 0.1 M $CuCl_2{\cdot}2H_2O$ precursor.

2.4. Trimethoprim photodegradation

Photocatalysts (20 mg) were dispersed in 50 mL of an aqueous trimethoprim (TMP) solution (0.103 mM) in a 250 mL glass photoreactor, with a quartz top plate for downward illumination, and sonicated for 5 min to ensure complete dispersion. The reactor was then kept in the dark, held at 25 °C using an EYELA NCB-1200 cooling system (Tokyo Rika Instruments), and stirred continuously at 500 rpm for 60 min to equilibrate any TMP adsorption, the extent of which was quantified by HPLC analysis of a 1 mL aliquot. Photocatalysis was initiated using a USHIO Optical Module X 500 W Xe lamp and 420 nm cutoff filter to ensure only visible light illumination; light intensity within the reactor was 1.82 mW/cm^2, with an effective irradiation area of 4.5 cm^2, and a reaction mixture to light source distance of 14.9 cm. Aliquots were periodically withdrawn from the mixture using a syringe, and filtered using a CPO20AN filter. The TMP removal efficiency was calculated according to **Equation 3**

$$\text{TMP removal (\%)} = \frac{\text{TMP initial} - \text{TMP final}}{\text{TMP initial}} \times 100 \qquad \textbf{3}$$

where initial and final denote the molar concentrations of TMP.

TMP was analyzed using a JASCO UV Plus 2075 series HPLC with an intelligent UV–vis detector at λ = 254 nm and Shodex C18M 4E analytical column (4.6 mm i.d. × 250 mm) with separation factors $\alpha 1$ = 2.42 and $\alpha 2$ = 1.47 held at 25 °C. The eluent consisted of 60:10:30 (v/v) acetonitrile: water: formic acid (25 mM) (TCI, Japan) with a flow rate of 0.6 mL/min; the maximum and minimum pressures were 20 and 0.2 MPa, respectively. The HPLC was calibrated for TMP prior to photocatalysis.

3. Results and discussion

3.1. Photophysical properties

The synthesis of a hierarchical Cu_2O-B nanoparticle aggregate is summarised in **Scheme 1.** Copper acetate is first dissolved to form a blue Cu^{2+} solution. Cu(II) ions are subsequently precipitated as the corresponding hydroxide on NaOH addition and partially reduced to a Cu_2O phase by ascorbic acid, and undergo a complex particle-mediated crystallization process, that likely involves Ostwald ripening and self-aggregation, to form Cu_2O nanoparticle aggregates under sonication. The use of an acetate precursor may be important in forming the final architecture since ($-COO^-$) ions may act as counterions or structure-directing agents when interacting with metal oxides, helping to stabilize unique nanostructures [42], [43].

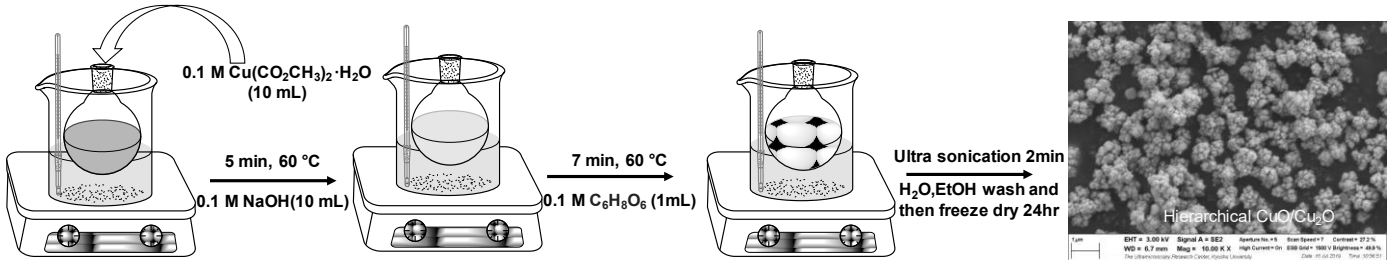

Scheme 1. Synthesis of hierarchical Cu_2O-B photocatalyst.

The role of copper precursor was explored by modifying the synthesis to use either sulfate (Cu_2O-C) or chloride (Cu/Cu_2O-F); different anions are expected to favour the growth of different crystal facets [44]. The choice of reductant, expected to influence the reduction kinetics and hence Cu(I)/Cu(II) speciation, was also studied by switching from ascorbic acid to hydrazine (Cu_2O-A) or hydroxylamine (Cu_2O-D). The impact of simultaneously changing copper precursor (to sulfate) and reductant (to hydroxylamine) was also investigated (Cu_2O-D).

Textural properties reveal Cu_2O materials were non-porous (**Fig. S2**) with low BET surface areas in all cases of between 7 and 21 $m^2.g^{-1}$ (**Table 1**). The phase purity of as-synthesized Cu_2O materials was characterized by powder X-ray diffraction (XRD) (**Fig. 1a**). Cu_2O-A and Cu_2O-B exhibited reflections at 29.6°, 36.4°, 42.4°, 51.8°, 61.5° and 73.5° corresponding to hkl planes (110), (111), (200), (211), (220) and (311) of Cu_2O (*Pn-3m* with space group) with unit cell parameters of a = 4.26, b = 4.26, c = 4.26 and β = 90.38. XRD patterns for Cu_2O-C and Cu_2O-D exhibited additional weak reflections characteristic of CuO, and for Cu_2O-D and Cu_2O-E weak reflections for $Cu_2(OH)_3Cl$ [22] or $Cu(OH)_2$, while Cu/Cu_2O-F comprised Cu_2O alongside trace copper metal. Volume-average crystallite sizes calculated from the Scherrer equation varied from 11 to 34 nm (**Table 1**); larger sizes are attributed to faster reduction and/or particle-mediated nucleation [15, 22].

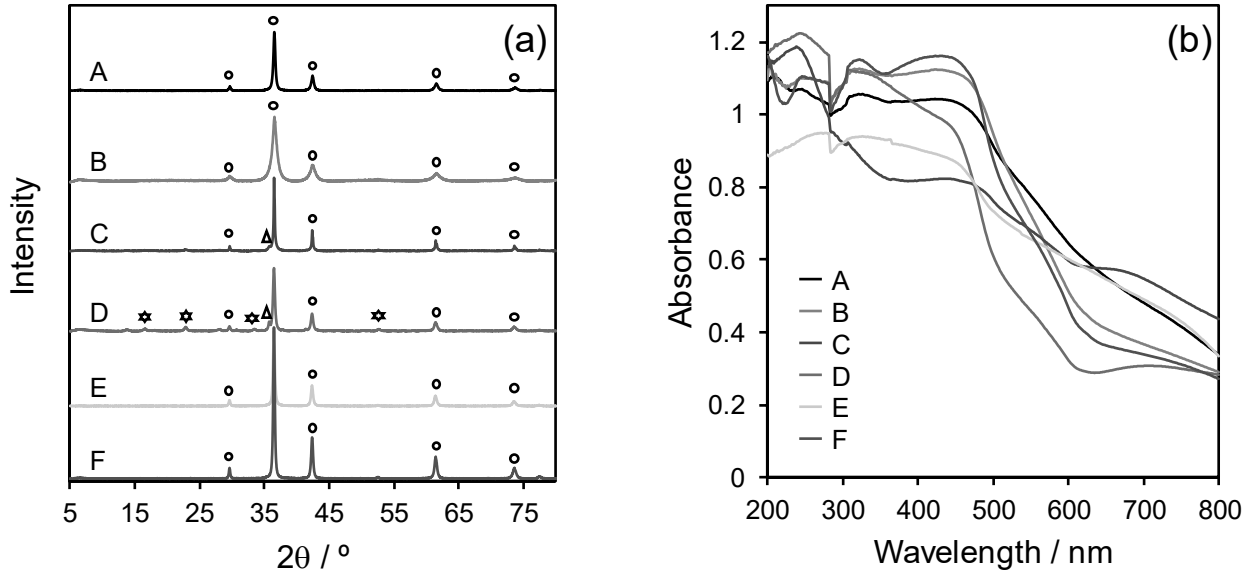

Fig. 1. (a) Powder XRD patterns with Cu_2O (○), CuO (△), $Cu(OH)_2$ (✡) reflections indicated, and (b) DRUV spectra of Cu_2O photocatalysts.

Optoelectronic properties of the Cu_2O materials were determined by solid state diffuse reflectance UV-Vis spectroscopy (DRUVS, **Fig. 1b**). In all cases a strong absorbance was observed below 500 nm, in accordance with previous reports on Cu_2O nanostructures [32], however the band edge was sensitive to the synthetic method, varying between 500 nm for Cu_2O-D to 600 nm for Cu_2O-A. Direct band gaps (E_g) determined from Tauc plots (**Fig. S1**) correspondingly vary across the Cu_2O materials from 2.1 eV for Cu_2O-C to 2.45 eV for Cu_2O-E respectively (**Table 1**), spanning a similar range to literature reports for Cu_2O nanostructures 2.17 eV to 2.69 eV [23, 45, 46]. Semiconductor band gaps are sensitive to particle size due to quantum confinement effects [47], and morphology [22, 46, 48], and hence variations in the electronic properties of the Cu_2O materials may reflect structural and/or compositional differences [49]. The DRUVS data also show the presence of additional weak absorption bands between 200-400 nm, attributed to electron transitions from deep valence band (VB) states into the conduction band (CB) [50],[51].

Field emission scanning electron microscopy (FESEM) and high-resolution transmission electron microscopy (HRTEM) analysis provide further insight into structural properties of the Cu_2O materials. In all cases, uniform nanostructures were obtained, however particle morphology and size were strongly dependent on the synthetic protocol. Cu_2O-A, Cu_2O-B and Cu_2O-C comprised approximately spherical aggregates (400 nm to 1600 nm diameter) of smaller (50 nm to 300 nm diameter) truncated cuboctahedral crystallites (**Fig. 2** and **S3**). The smallest aggregates and constituent crystallites were obtained for Cu_2O–B (**Table 1**). In contrast, Cu_2O-D, Cu_2O-E and Cu_2O-F appeared as compact spherical (~400 nm) or cubic (400 nm or 1600 nm) particles.

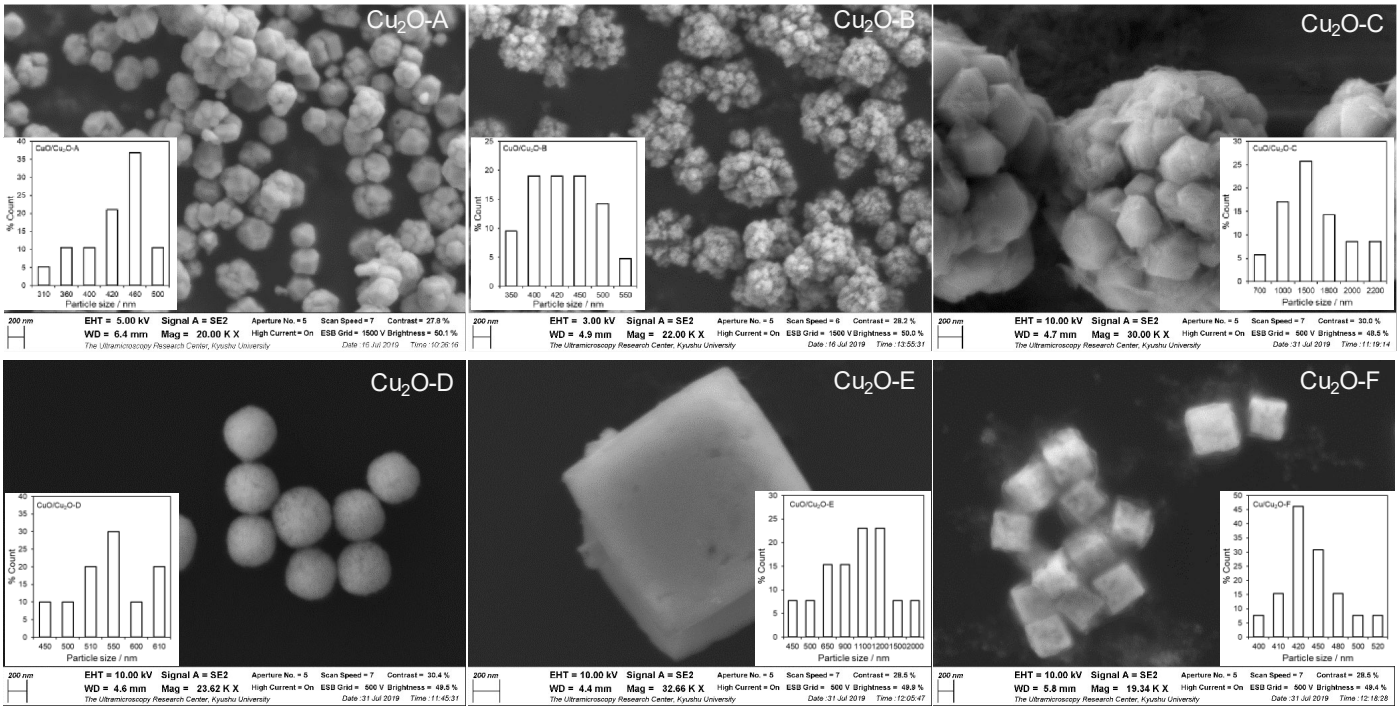

Fig. 2. FESEM images and corresponding particle size distributions (inset) of Cu_2O photocatalysts.

Table 1. Physicochemical properties of synthesized Cu_2O catalysts.

Sample	Crystal size / nm[a]	Particle size[b]		BET surface area[c] / $m^2.g^{-1}$	Band gap / eV[d]	VB edge[e] / eV	CB edge[f] / eV	Surface Cu(I)[g] / %
		Aggregate	Individual					
Cu_2O-A	26	460	100-130	7	2.19	1.0	-1.19	16
Cu_2O-B	11	410	50-80	10	2.20	1.5	-0.70	72
Cu_2O-C	34	1600	200-300	20	2.10	1.0	-1.10	22
Cu_2O-D	27	538	-	21	2.40	0.5	-1.90	66
Cu_2O-E	30	1230	-	13	2.45	1.5	-0.95	41
Cu_2O-F	33	450	-	13	2.29	1.2	-1.09	52

[a]XRD. [b]FESEM/HRTEM. [c]N_2 porosimetry. [d]DRUVS. [e]VB XPS. [f]VB XPS and DRUVS. [g]XPS

HRTEM confirmed that Cu_2O-A, Cu_2O-B and Cu_2O-C exhibited hierarchical structures whereas Cu_2O-D, Cu_2O-E and Cu_2O-F exhibited compact, single particle morphologies (**Fig. 3**). Average Cu:O stoichiometries determined by EDX (**Fig. S4**) varied between 2.3:1 to 2.7:1 in fair agreement with a Cu_2O stoichiometry, albeit evidencing some additional (non-oxygen containing) copper phases, except for Cu_2O-E for which the presence of significant CuO or $Cu(OH)_2$ was indicated. Elemental mapping (**Fig. 3** and **Fig. S4-S5**) suggests a fairly uniform composition throughout all aggregates and particles.

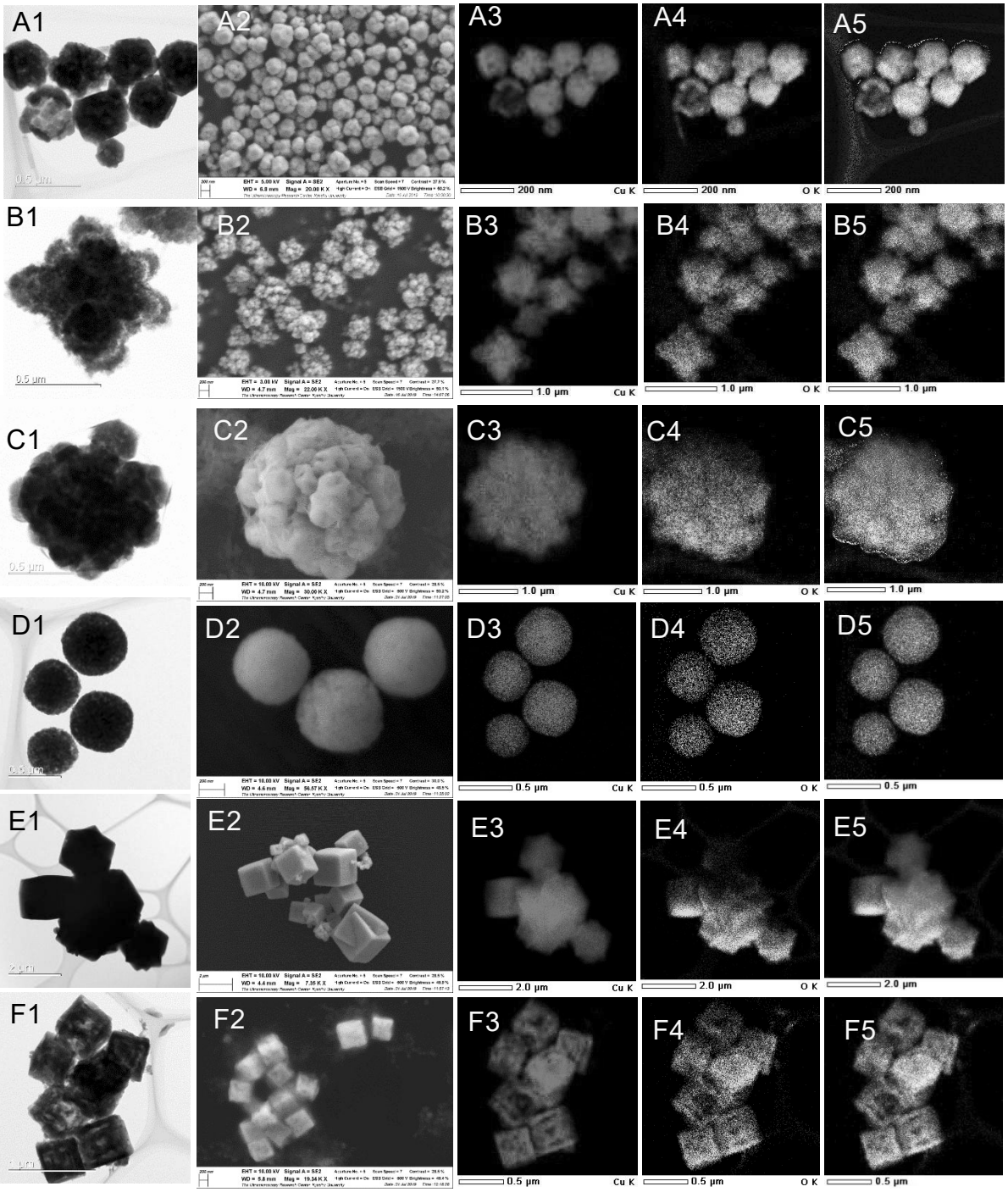

Fig. 3. HRTEM, SEM, elemental, and EDX mapping of Cu_2O photocatalysts: Cu_2O-A (A1–A5), Cu_2O-B (B1–B5), Cu_2O-C (C1–C5), Cu_2O-D (D1–D5), Cu_2O-E (E1–E5), and Cu_2O-F (F1–F5).

Electronic structure analysis by electron energy loss spectroscopy (EELS) provides a more sensitive local probe of the copper chemical environment and can readily differentiate CuO and Cu_2O phases based on the Cu L_3:Cu L_2 intensity ratio and line shape [52]. EELS analysis of the surface of individual particles within Cu_2O-B aggregates reveals a Cu_2O rich surface, in contrast to the CuO corona previously observed for Cu_2O@CuO core-shell nanoparticle aggregates synthesized using a PEG structure-directing agent. Lattice fringes of 0.24 nm for (111) planes at the surface of individual particles are also indicative of Cu_2O (**Fig. 4e** and **Fig. S6**). The relative stability of copper oxides is size dependent, with cubic Cu_2O more stable <25 nm

than monoclinic CuO [53], and a function of oxygen exposure [54], in accordance with the volume-averaged Cu_2O crystallite size of ~11 nm for Cu_2O-B (**Table 1**).

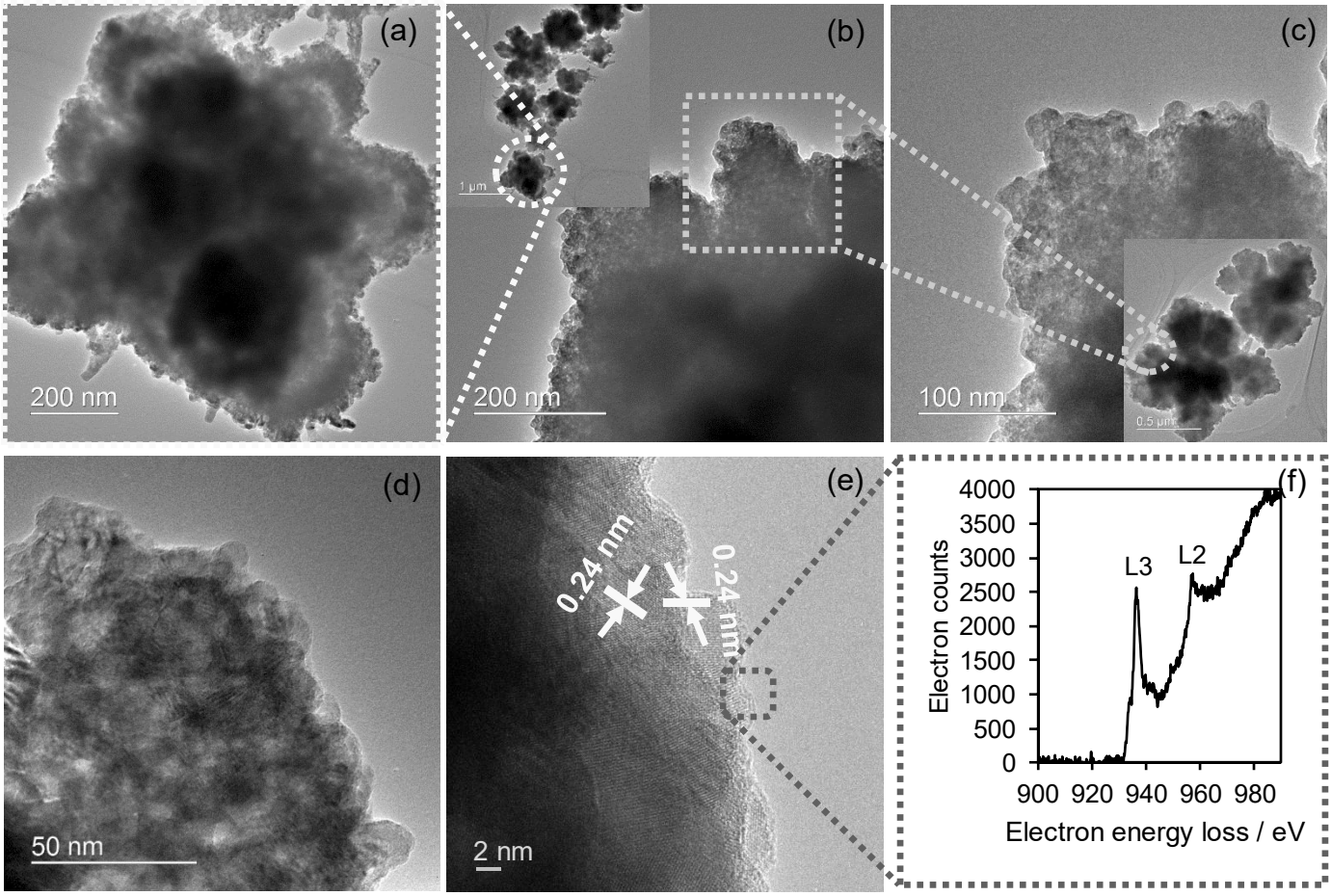

Fig. 4. (a)–(e) High-resolution TEM images and (d, insert) and (f) corresponding EELS spectrum of Cu_2O-B photocatalyst.

The surface oxidation states of Cu_2O materials were determined by fitting of Cu 2p XP spectra (**Fig. 5**) which exhibited spin-orbit split $2p_{3/2}$ and Cu $2p_{1/2}$ peaks at approximately 932 and 952 eV binding energies respectively, along with weaker shake-up satellite features at 942 eV and 962 eV [55]. Fitting revealed two distinct copper environments with $2p_{3/2}$ binding energies at 931.6 eV and 933.9 eV indicative of Cu_2O and $Cu(OH)_2$ respectively [56]; note that the 942 eV satellite lineshape is also characteristic of Cu(II) hydroxide not oxide. Cu_2O-B exhibited the highest concentration of surface Cu_2O, consistent with EELS and HRTEM measurements (**Table 1**), whereas Cu_2O-A, Cu_2O-C and Cu_2O-E exhibited the lowest Cu_2O concentrations, in fair agreement with average and local Cu:O bulk stoichiometries from EDX analysis (**Fig. S4-S5**). Corresponding valence band (VB) XP spectra (**Fig. S7**) enable estimation of the VB maximum (edge potential) from the intercept of a tangent to the density of states at the Fermi edge (**Fig. S7**), and conduction band (CB) minimum in combination with band gap information from DRUVS. VB maxima spanned 0.5 eV to 1.5 eV, while CB spanned -0.7 to -1.9 eV, similar to literature reports for Cu_2O nanoparticles [32, 57, 58]. The VB maxima are significantly higher than required to generate reactive oxygen species (-0.16 V at pH 7 [59]) and also sufficient to split water [32].

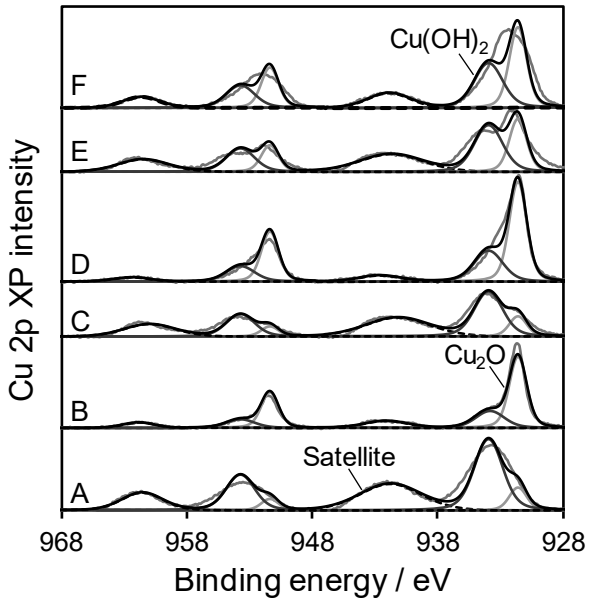

Fig. 5. Cu 2p XP spectra of Cu_2O photocatalysts.

Copper speciation throughout Cu_2O materials was subsequently explore by XANES analysis of Cu K-edge transmission spectra and linear combination fitting against reference compounds. In all cases, spectra exhibited a pre-edge feature at 8981 eV, assigned to the electric dipole-allowed transition characteristic of Cu(I), with no evidence of the 8984 eV feature characteristic of the 1s → 4p "shake down" transition of Cu(II) [60]. In all cases, Cu_2O was the dominant phase, as expected from XRD and EDX, with Cu_2O-B and Cu_2O-F containing the least Cu(II) species whereas Cu_2O-E contained the most Cu(II) species (**Fig. 6** and **Table 2**) present as either CuO or $Cu(OH)_2$.

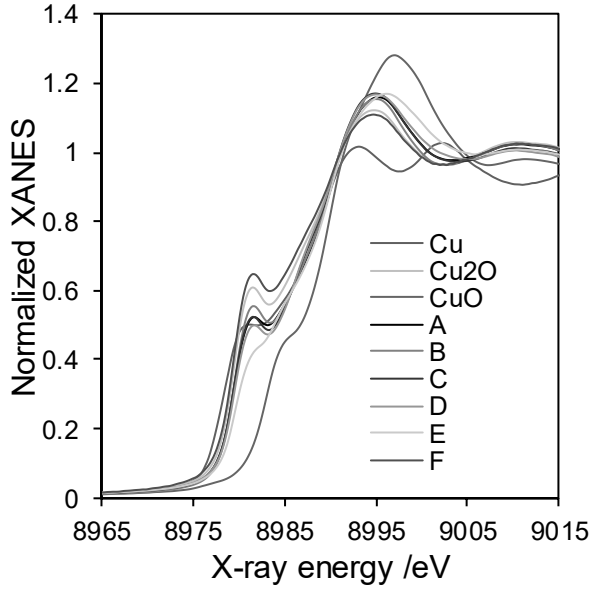

Fig. 6. Cu K-edge XANES spectra of Cu_2O photocatalysts and references.

Table 2. XANES linear combination fitting of Cu_2O photocatalysts.

Sample	Cu_2O	CuO (or $Cu(OH)_2$)	Cu metal	R factor x 10^{-4}	χ^2 x 10^{-4}
Cu_2O-A	79	21	0	2.9	0.6
Cu_2O-B	85	15	0	7.9	0.2
Cu_2O-C	81	19	0	8.5	0.2
Cu_2O-D	76	24	0	8.2	0.2
Cu_2O-E	59	41	0	3.5	0.8
Cu_2O-F	92	0	8	4.4	0.8

3.2. Photocatalytic TMP oxidation

The photocatalytic degradation of TMP was investigated over Cu_2O photocatalysts under visible light ($\lambda \geq$ 420 nm) irradiation, and to our knowledge is the first study of copper for the photodegradation of this antibiotic. Equilibration in the dark established that TMP adsorption was negligible over any of Cu_2O photocatalysts, and TMP underwent minimal photolysis (<3 % conversion) under our reaction conditions. Note that TMP exhibits strong UV absorption (290 nm maximum) and hence is very sensitive to photolysis under UV light, the irradiation source employed in all previous literature photocatalytic studies. Initial rates of degradation for 0.103 mM TMP, a similar concentration to previous studies [36, 61], varied widely across the Cu_2O photocatalysts (**Fig. 7a**), being fastest for Cu_2O-B (1.12 $\mu mol.g^{-1}.min^{-1}$) and slowest for Cu_2O-C, Cu_2O-D, Cu_2O-E and Cu_2O-F (0.26-0.4 $\mu mol.g^{-1}.min^{-1}$); trends in surface area normalised rate (**Fig. 7b**) mirrored specific activity. Performance benchmarking against literature catalysts for TMP photocatalytic degradation (**Table 3**) demonstrates that Cu_2O-B is significantly more active than most previous studies, despite our use of visible light. The only studies reporting greater activity in **Table 3** used high power UV [36, 62, 63] and/or high energy UV-C [41] irradiation and are hence do not represent low energy, low cost scalable technologies and are likely compromised by significant photolysis. Specific activity across the family of Cu_2O photocatalysts shows a strong inverse correlation with Cu_2O crystallite size (**Fig. 7c**), indicating that bulk recombination of photogenerated charge carriers plays a significant role in controlling TMP degradation. TMP removal for Cu_2O-B was 48 % after 5 h reaction. The most active Cu_2O-B hierarchical nanostructure is also promising for the photocatalytic degradation of N-acetyl-para-aminophenol and phenol (**Fig. S8**), important recalcitrant organic compounds that pollute wastewater.

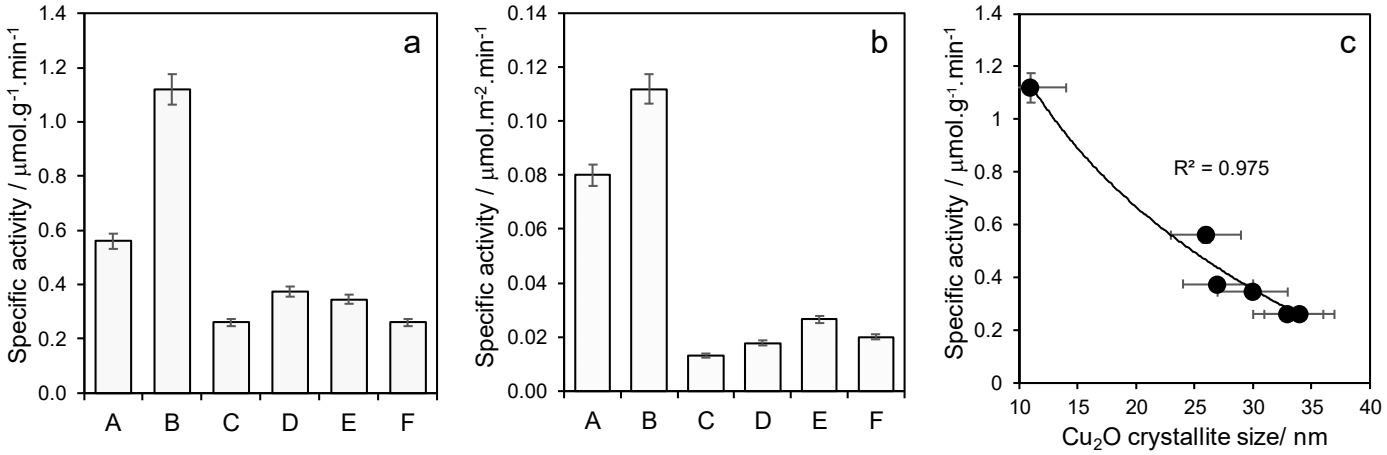

Fig. 7. (a) Specific activity and (b) surface area normalised specific activity for TMP photocatalytic degradation over Cu_2O catalysts under visible light, and (c) correlation between specific activity and Cu_2O crystallite size. Reaction conditions: 0.103 mM TMP, 50 mL water, 20 mg catalyst, 60 min reaction.

Table 3. Photocatalytic TMP degradation under visible and/or UV irradiation.

Photocatalyst	Reaction conditions	Light source		Specific activity / µmol.g^{-1}.min^{-1}	Reference
		Type	Properties		
Hierarchical CuO/Cu_2O	20 mg catalyst, 50 mL of 0.103 mM TMP	Visible	500 W Xe lamp, λ>400 nm, 1.82 mW/cm^2	1.12	This work
TiO_2-P25	200 mg catalyst, 1 L of 0.068 mM TMP	UV	λ< 400 nm, 3 mW/cm^2	11.90	[36]
TiO_2-P25	500 mg catalyst, 1 L of 0.35 mM TMP	UV-Vis	1500 W Xe lamp, λ>280 nm	6.90	[62]
TiO_2-P25	50 mg catalyst, 1 L of 0.0034 mM TMP, in flow	UV-A	LED lamp, 4320 mWs/cm^2	2.86	[63]
TiO_2-P25	250 mg catalyst, 250 mL of 0.136 mM TMP	UV-C	254 nm	0.25	[64]
Ag/TiO_2-P25	250 mg catalyst, 250 mL of 0.136 mM TMP	UV-C	254 nm	0.58	[64]
Ni/TiO_2-P25	250 mg catalyst, 250 mL of 0.136 mM TMP	UV-C	254 nm	0.33	[64]
S-TiO_2-anatase	50 mg catalyst, 100 mL of 0.034 mM TMP	UV-Vis	400 W metal halide lamp, 220 µW/cm^{-2}	0.34	[65]
NiO_x/organic aerogel	8 mg catalyst, 800 mL of 0.01 mM TMP	UV-C /UV-A	11 W Hg vapour lamp, 254 nm or 315-400 nm	10.00	[41]
Ru/WO_3/ZrO_2	50 mg catalyst, 100 mL of 0.034 mM TMP	UV-Vis	400 W metal halide lamp, UV-Vis light, 0.22 mW/cm^{-2}	0.49	[65]

Further insight into photogenerated charge carrier recombination was obtained from photoluminescence (PL) spectroscopy (**Fig. 8a-b**). The PL spectra of Cu_2O photocatalysts excited by 380 nm or 560 nm light exhibited characteristic Cu_2O emissions ~531 nm and 610 nm respectively [66, 67]. The PL intensities were

lowest for Cu_2O-A and Cu_2O-B in both cases, indicative of slower radiative recombination compared to the other catalysts [22], and consistent with the hypothesis that the smaller Cu_2O crystallite sizes in these two photocatalysts is responsible for their superior degradation activity (**Fig. 7c**). Conversely Cu_2O-C, Cu_2O-E and Cu_2O-F, possessing the largest crystallite sizes, exhibited the greatest fluorescence due to recombination.

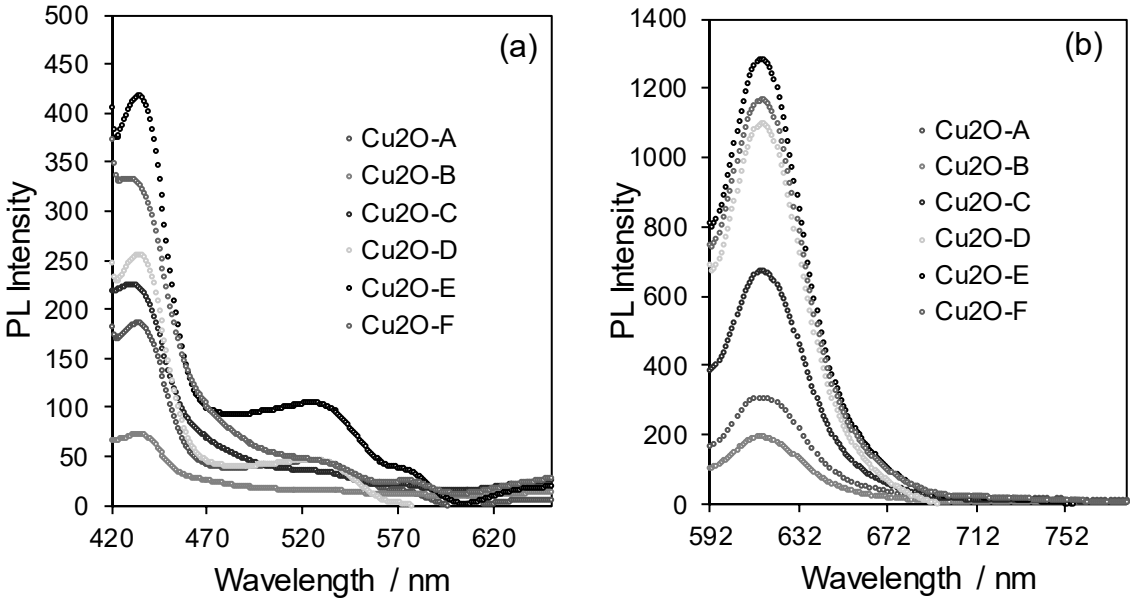

Fig. 8. PL spectrum of Cu_2O photocatalysts. (a) Excitation at 380 nm. (b) Excitation at 560 nm. PL spectrum measurement conditions: excitation bandwidth = 2 nm, emission bandwidth = 5 nm, response = 0.5 s, photomultiplier tube voltage = 800 V, scan speed = 200 nm/min.

The photostability of the most active Cu_2O-B photocatalyst was investigated post-reaction. XRD (**Fig. 9a**) confirmed retention of phase pure Cu_2O crystallites, although XPS revealed partial surface disproportionation, evidenced by a new Cu 2p XP peak at 929.9 eV and simultaneous growth and change in lineshape of the Cu(II) satellite at 941 eV (**Fig. 9b**), indicative of Cu metal and CuO respectively[68]. Nevertheless, visible light activity for TMP oxidation remained almost constant over five consecutive reaction cycles (25 h total) (**Fig. 9c**).

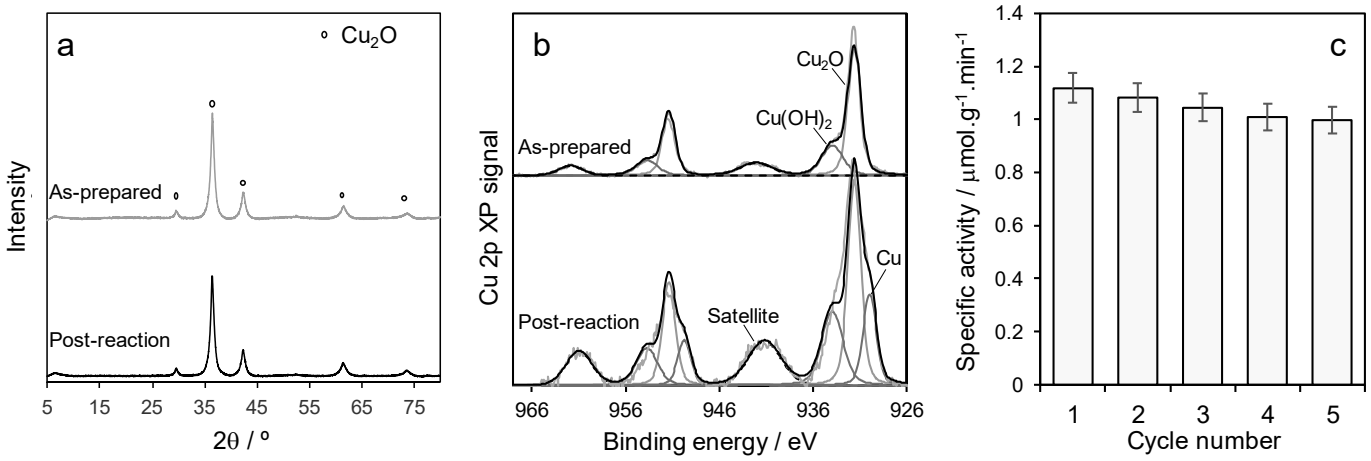

Fig. 9. (a) XRD patterns and (b) Cu 2p XP spectra of as-prepared and post-reaction Cu_2O-B photocatalyst, and (c) specific activity for TMP photocatalytic degradation over Cu_2O-B under visible light irradiation as a function of reaction cycle.

The active species responsible for TMP photodegradation over the Cu_2O-B photocatalyst was examined by fluorescence spectroscopy using terephthalic acid (TA) as probe molecule (**Fig. 10**). TA reacted with photogenerated $^{\bullet}OH$ radicals, evidenced by the appearance of a 425 nm emission (under 315 nm excitation) characteristic of 2-hydroxyterephthalic acid (HTA). The HTA concentration increased monotonically with irradiation time, consistent with an increase in hydroxyl radical concentration. It therefore appears that Cu_2O-B is an effective photocatalyst for hydroxyl radical ($^{\bullet}OH$) production, in accordance with previous reports that TMP photodegradation is catalysed by $^{\bullet}OH$ [63, 65, 69]. ESR spin trapping experiments using 5,5-dimethyl-1-pyrrolidine N-oxide (DMPO) provide direct evidence for $^{\bullet}OH$ production over Cu_2O-B photocatalyst under visible light illumination (**Fig. S9**) resulting in a DMPO-$^{\bullet}OH$ adduct. Additional hole scavenger experiments suggest superoxide radicals is unlikely to play a significant role in TMP photodegradation. A possible mechanism for hydroxyl radical generation is summarised in **Eqs. 4-10** below:

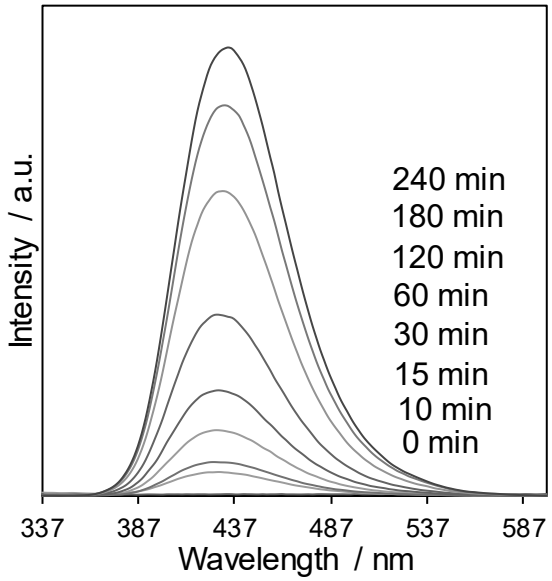

Fig. 10. PL spectroscopy of terephthalic acid in the presence of Cu_2O-B photocatalyst.

$$Cu_2O + hv \rightarrow Cu_2O^*(h^+_{VB} + e^-_{CB}) \quad \textbf{4}$$

$$Cu_2O^*\ (h^+_{VB}) + H_2O \rightarrow Cu_2O\ (HO^{\cdot}) + H^+ \quad \textbf{5}$$

$$Cu_2O^*(e^-_{CB}) + O_2 \rightarrow Cu_2O(O_2^{-\cdot}) \quad \textbf{6}$$

$$Cu_2O(O_2^{-\cdot}) + H^+ \rightarrow Cu_2O^*(HO_2^{\cdot}) \quad \textbf{7}$$

$$Cu_2O^*(HO_2^{\cdot}) + Cu_2O^*(HO_2^{\cdot}) \rightarrow Cu_2O(H_2O_2) + O_2 \quad \textbf{8}$$

$$Cu_2O(H_2O_2) + hv \rightarrow Cu_2O^*(2HO^{\cdot}) \quad \textbf{9}$$

$$Cu_2O^*(HO^{\cdot}) + TMP + hv \rightarrow intermediates + H_2O \quad \textbf{10}$$

LC-MS analysis of the reaction mixture (**Fig. S10-S13**) revealed the formation of a series of products from TMP (**I**). The primary product during the first hour of reaction (**II**), with *m/z* 307, may arise from hydroxylation of an aromatic ring or aliphatic carbon; in the latter scenario further oxidation may form the ketone (**III**). Additional products (IV-VII), with *m/z* values of 197, 155 and 143 respectively, appeared >2 h reaction and are consistent with monocylic fragments of the parent TMP molecule arising from further hydroxylation, oxidation and/or demethylation [36].

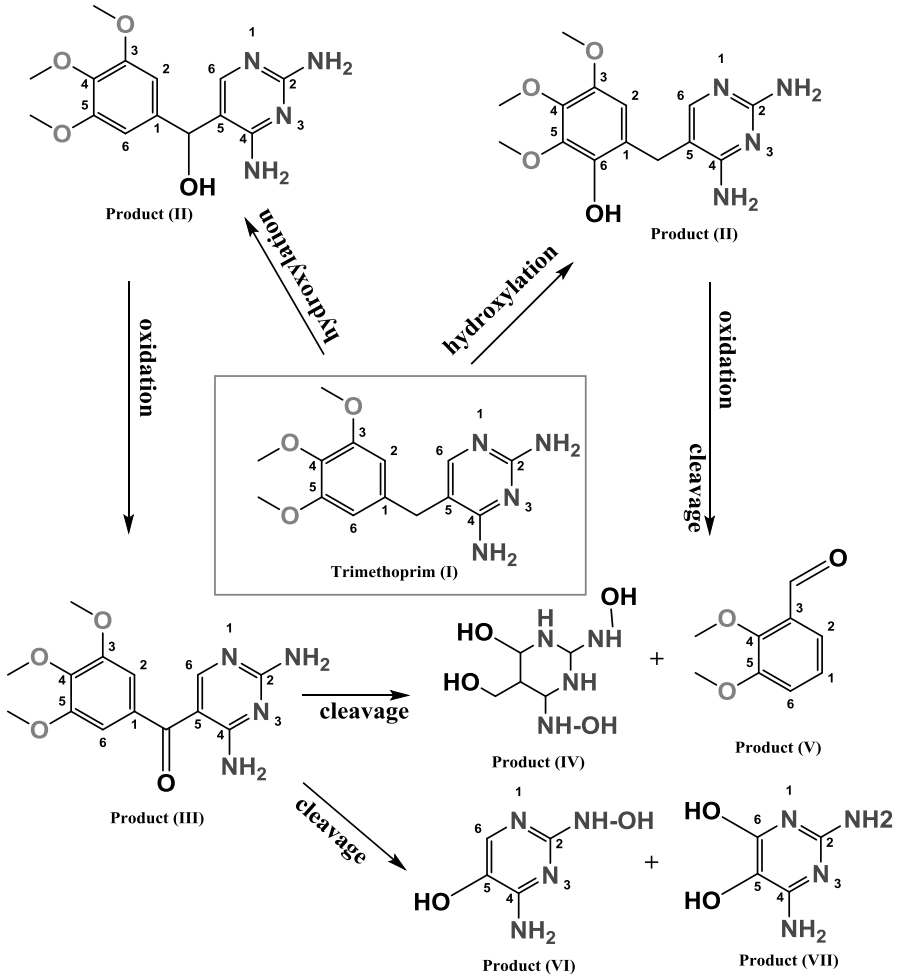

Scheme 2. Proposed reaction mechanism for TMP photocatalytic degradation over Cu_2O photocatalysts.

4. Conclusions

We demonstrate a one-pot, surfactant-free, hydrothermal synthesis of Cu_2O nanostructures for the visible light photocatalytic degradation of trimethoprim, an archetypal xenobiotic, in water. The choice of copper precursor (acetate, sulfate or chloride) and reductant (ascorbic acid, hydroxylamine or hydrazine) had little impact on the resulting bulk phase formed, which XRD, TEM and XAS evidenced as Cu_2O in all cases. However, the synthetic parameter strongly influenced the nanostructure morphology, which varied from compact hierarchical aggregates of ~400 nm (comprised of 11 nm Cu_2O crystallites nucleated as 50-80 particles) to essentially non-porous nanocubes of 1230 nm (comprised of fused 30 nm Cu_2O crystallites). Photophysical characterization of Cu_2O nanostructures by DRUVS, XPS, EELS and photoluminescence spectroscopy revealed significant, but not systematic, variations in the band gap, band energies and surface speciation of copper. Promising initial rates and 5 h removal efficiencies were observed for the oxidative degradation of TMP under visible light for the hierarchical nanostructure possessing the smallest Cu_2O crystallites (Cu_2O-B), which are comparable to those reported under high intensity and/or energy UV irradiation. Mechanistic studies using LC-MS and the oxidation of terephthalic acid (TA) as a probe reaction, identified hydroxyl radicals as the key reactive oxygen species responsible for TMP photodegradation over Cu_2O-B; reaction proceeds through hydroxylation to bicyclic intermediates and their subsequent oxidative cleavage to monocyclic fragments. The hierarchical Cu_2O-B photocatalyst exhibited excellent stability for TMP degradation over 25 h. These new insights may help guide the design of improved low cost and sustainable semiconductor photocatalysts for environmental remediation and applications in solar fuels production.

Supporting information

Catalyst characterization: **Fig. S1.** Tauc plots of synthesised Cu_2O photocatalysts; **Fig. S2.** N_2 adsorption-desorption isotherms and BJH pore size distributions of Cu_2O photocatalysts; **Fig. S3.** Low resolution FE-SEM images of Cu_2O photocatalysts; **Fig. S4.** EDX elemental maps and corresponding bulk compositions of Cu_2O photocatalysts; **Fig. S5.** Bright field TEM images and intraparticle elemental gradients of Cu_2O photocatalysts; **Fig. 6 (a-b**) High-resolution TEM images of Cu_2O-B; **Fig. S7.** Cu 2p valence band XP spectrum of synthesised Cu_2O catalysts; **Fig. S8.** Results for additional pollutants. **Fig. S9.** EPR spin trapping over Cu_2O-B photocatalyst using DMPO as a radical trapping probe molecule; **Fig. S10.** LC-MS/MS spectra of TMP; **Fig. S11-S13.** LC-MS/MS spectra of TMP products over Cu_2O-B catalyst under visible light irradiation.

Conflicts of interest

The authors declare no conflict of interest.

ACKNOWLEDGMENTS

S. K. and K. S. would like to thank the Japan Society for the Promotion of Science (JSPS) for providing a postdoctoral fellowship for foreign researchers (P18387) and the research grant (KAKENHI JP18F18387). XANES measurements were performed at Kyushu University Beamline (SAGA-LS/BL06 with proposal No. 2019IIIK005). FE-SEM and HR(S)TEM performed at the Ultra-microscopy Research Centre (URC) at Kyushu University. This work was partly supported by Nanotechnology Platform Program (Molecule and Material Synthesis) of the Ministry of Education, Culture, Sports, Science and Technology (MEXT), Japan.

REFERENCES

[1] H. Zhang, Q. Zhu, Y. Zhang, Y. Wang, L. Zhao, B. Yu, One-Pot Synthesis and Hierarchical Assembly of Hollow Cu2O Microspheres with Nanocrystals-Composed Porous Multishell and Their Gas-Sensing Properties, Advanced Functional Materials, 17 (2007) 2766-2771, 10.1002/adfm.200601146.

[2] C.M. Parlett, K. Wilson, A.F. Lee, Hierarchical porous materials: catalytic applications, Chemical Society Reviews, 42 (2013) 3876-3893, 10.1039/c2cs35378d.

[3] X. Li, J. Yu, M. Jaroniec, Hierarchical photocatalysts, Chemical Society Reviews, 45 (2016) 2603-2636, 10.1039/C5CS00838G.

[4] W. Zhan, Y. Yuan, L. Sun, Y. Yuan, X. Han, Y. Zhao, Hierarchical NiO@N-Doped Carbon Microspheres with Ultrathin Nanosheet Subunits as Excellent Photocatalysts for Hydrogen Evolution, Small, 15 (2019) 1901024, 10.1002/smll.201901024.

[5] F. Lu, W. Cai, Y. Zhang, ZnO Hierarchical Micro/Nanoarchitectures: Solvothermal Synthesis and Structurally Enhanced Photocatalytic Performance, Advanced Functional Materials, 18 (2008) 1047-1056, 10.1002/adfm.200700973.

[6] Y. Huo, J. Zhang, M. Miao, Y. Jin, Solvothermal synthesis of flower-like BiOBr microspheres with highly visible-light photocatalytic performances, Applied Catalysis B: Environmental, 111-112 (2012) 334-341, https://doi.org/10.1016/j.apcatb.2011.10.016.

[7] G. Zhou, X. Xu, T. Ding, B. Feng, Z. Bao, J. Hu, Well–Steered Charge–Carrier Transfer in 3D Branched CuxO/ZnO@Au Heterostructures for Efficient Photocatalytic Hydrogen Evolution, ACS Applied Materials & Interfaces, 7 (2015) 26819-26827, 10.1021/acsami.5b09027.

[8] R. Wang, J. Guo, D. Chen, Y.-E. Miao, J. Pan, W.W. Tjiu, T. Liu, “Tube brush” like ZnO/SiO2 hybrid to construct a flexible membrane with enhanced photocatalytic properties and recycling ability, Journal of Materials Chemistry, 21 (2011) 19375-19380, 10.1039/C1JM13979G.

[9] J.H. Pan, X.Z. Wang, Q. Huang, C. Shen, Z.Y. Koh, Q. Wang, A. Engel, D.W. Bahnemann, Large-scale Synthesis of Urchin-like Mesoporous TiO2 Hollow Spheres by Targeted Etching and Their Photoelectrochemical Properties, Advanced Functional Materials, 24 (2014) 95-104, 10.1002/adfm.201300946.

[10] M.B. Gawande, A. Goswami, F.-X. Felpin, T. Asefa, X. Huang, R. Silva, X. Zou, R. Zboril, R.S. Varma, Cu and Cu-Based Nanoparticles: Synthesis and Applications in Catalysis, Chemical Reviews, 116 (2016) 3722-3811, 10.1021/acs.chemrev.5b00482.

[11] C. Kim, K.M. Cho, A. Al-Saggaf, I. Gereige, H.-T. Jung, Z-scheme Photocatalytic CO2 Conversion on Three-Dimensional BiVO4/Carbon-Coated Cu2O Nanowire Arrays under Visible Light, ACS Catalysis, 8 (2018) 4170-4177, 10.1021/acscatal.8b00003.

[12] Y. Zhang, B. Deng, T. Zhang, D. Gao, A.-W. Xu, Shape Effects of Cu2O Polyhedral Microcrystals on Photocatalytic Activity, The Journal of Physical Chemistry C, 114 (2010) 5073-5079, 10.1021/jp9110037.

[13] T. Wei, Y.-N. Zhu, X. An, L.-M. Liu, X. Cao, H. Liu, J. Qu, Defect Modulation of Z-Scheme TiO2/Cu2O Photocatalysts for Durable Water Splitting, ACS Catalysis, 9 (2019) 8346-8354, 10.1021/acscatal.9b01786.

[14] D. Ren, Y. Deng, A.D. Handoko, C.S. Chen, S. Malkhandi, B.S. Yeo, Selective Electrochemical Reduction of Carbon Dioxide to Ethylene and Ethanol on Copper(I) Oxide Catalysts, ACS Catalysis, 5 (2015) 2814-2821, 10.1021/cs502128q.

[15] S. Karthikeyan, K. Ahmed, A. Osatiashtiani, A.F. Lee, K. Wilson, K. Sasaki, B. Coulson, W. Swansborough-Aston, R. Douthwaite, W. Li, Pompon Dahlia-like Cu2O/rGO nanostructures for visible light photocatalytic H2 production and 4-chlorophenol degradation, ChemCatChem, 12 (2020) 1699-1709, 10.1002/cctc.201902048.
[16] F.A.C. Pastrián, A.G.M. da Silva, A.H.B. Dourado, A.P. de Lima Batista, A.G.S. de Oliveira-Filho, J. Quiroz, D.C. de Oliveira, P.H.C. Camargo, S.I. Córdoba de Torresi, Why Could the Nature of Surface Facets Lead to Differences in the Activity and Stability of Cu2O-Based Electrocatalytic Sensors?, ACS Catalysis, 8 (2018) 6265-6272, 10.1021/acscatal.8b00726.
[17] S. Yoon, S.-D. Kim, S.-Y. Choi, J.-H. Lim, B. Yoo, Hierarchical Shape Evolution of Cuprous Oxide Micro- and Nanocrystals by Surfactant-Assisted Electrochemical Deposition, Crystal Growth & Design, 15 (2015) 4969-4974, 10.1021/acs.cgd.5b00873.
[18] Y.A. Wu, I. McNulty, C. Liu, K.C. Lau, Q. Liu, A.P. Paulikas, C.-J. Sun, Z. Cai, J.R. Guest, Y. Ren, Facet-dependent active sites of a single Cu 2 O particle photocatalyst for CO 2 reduction to methanol, Nature Energy, 4 (2019) 957-968, 10.1038/s41560-019-0490-3.
[19] W.-C. Huang, L.-M. Lyu, Y.-C. Yang, M.H. Huang, Synthesis of Cu2O Nanocrystals from Cubic to Rhombic Dodecahedral Structures and Their Comparative Photocatalytic Activity, Journal of the American Chemical Society, 134 (2012) 1261-1267, 10.1021/ja209662v.
[20] R. Chen, S. Pang, H. An, J. Zhu, S. Ye, Y. Gao, F. Fan, C. Li, Charge separation via asymmetric illumination in photocatalytic Cu 2 O particles, Nature Energy, 3 (2018) 655-663, 10.1038/s41560-018-0194-0.
[21] C.-H. Kuo, M.H. Huang, Fabrication of Truncated Rhombic Dodecahedral Cu2O Nanocages and Nanoframes by Particle Aggregation and Acidic Etching, Journal of the American Chemical Society, 130 (2008) 12815-12820, 10.1021/ja804625s.
[22] S. Karthikeyan, C. Chuaicham, R.R. Pawar, K. Sasaki, W. Li, A.F. Lee, K. Wilson, Template free mild hydrothermal synthesis of core–shell Cu2O(Cu)@CuO visible light photocatalysts for N-acetyl-para-aminophenol degradation, Journal of Materials Chemistry A, 7 (2019) 20767-20777, 10.1039/C9TA07009E.
[23] C.-H. Kuo, C.-H. Chen, M.H. Huang, Seed-Mediated Synthesis of Monodispersed Cu2O Nanocubes with Five Different Size Ranges from 40 to 420 nm, Advanced Functional Materials, 17 (2007) 3773-3780, 10.1002/adfm.200700356.
[24] L. Wan, Q. Zhou, X. Wang, T.E. Wood, L. Wang, P.N. Duchesne, J. Guo, X. Yan, M. Xia, Y.F. Li, Cu 2 O nanocubes with mixed oxidation-state facets for (photo) catalytic hydrogenation of carbon dioxide, Nature Catalysis, 2 (2019) 889-898, 10.1038/s41929-019-0338-z.
[25] H. Yu, J. Yu, S. Liu, S. Mann, Template-free Hydrothermal Synthesis of CuO/Cu2O Composite Hollow Microspheres, Chemistry of Materials, 19 (2007) 4327-4334, 10.1021/cm070386d.
[26] K.X. Yao, X.M. Yin, T.H. Wang, H.C. Zeng, Synthesis, Self-Assembly, Disassembly, and Reassembly of Two Types of Cu2O Nanocrystals Unifaceted with {001} or {110} Planes, Journal of the American Chemical Society, 132 (2010) 6131-6144, 10.1021/ja100151f.
[27] A. Radi, D. Pradhan, Y. Sohn, K.T. Leung, Nanoscale Shape and Size Control of Cubic, Cuboctahedral, and Octahedral Cu−Cu2O Core−Shell Nanoparticles on Si(100) by One-Step, Templateless, Capping-Agent-Free Electrodeposition, ACS Nano, 4 (2010) 1553-1560, 10.1021/nn100023h.
[28] X. Bai, J. Wei, B. Tian, Y. Liu, T. Reiss, N. Guiblin, P. Gemeiner, B. Dkhil, I. C. Infante, Size effect on optical and photocatalytic properties in BiFeO3 nanoparticles, The Journal of Physical Chemistry C, 120 (2016) 3595-3601, 10.1021/acs.jpcc.5b09945.
[29] H. Li, Z. Su, S. Hu, Y. Yan, Free-standing and flexible Cu/Cu2O/CuO heterojunction net: A novel material as cost-effective and easily recycled visible-light photocatalyst, Applied Catalysis B: Environmental, 207 (2017) 134-142, https://doi.org/10.1016/j.apcatb.2017.02.013.
[30] R.-Y. Zhong, K.-Q. Sun, Y.-C. Hong, B.-Q. Xu, Impacts of Organic Stabilizers on Catalysis of Au Nanoparticles from Colloidal Preparation, ACS Catalysis, 4 (2014) 3982-3993, 10.1021/cs501161c.
[31] S. Roy, S. Roy, A. Rao, G. Devatha, P.P. Pillai, Precise Nanoparticle–Reactant Interaction Outplays Ligand Poisoning in Visible-Light Photocatalysis, Chemistry of Materials, 30 (2018) 8415-8419, 10.1021/acs.chemmater.8b03108.
[32] S. Karthikeyan, S. Kumar, L.J. Durndell, M.A. Isaacs, C.M.A. Parlett, B. Coulson, R.E. Douthwaite, Z. Jiang, K. Wilson, A.F. Lee, Size-Dependent Visible Light Photocatalytic Performance of Cu2O Nanocubes, ChemCatChem, 10 (2018) 3554-3563, 10.1002/cctc.201800439.
[33] M. Zabilskiy, P. Djinović, E. Tchernychova, O.P. Tkachenko, L.M. Kustov, A. Pintar, Nanoshaped CuO/CeO2 Materials: Effect of the Exposed Ceria Surfaces on Catalytic Activity in N2O Decomposition Reaction, ACS Catalysis, 5 (2015) 5357-5365, 10.1021/acscatal.5b01044.

[34] Y. Kwon, A. Soon, H. Han, H. Lee, Shape effects of cuprous oxide particles on stability in water and photocatalytic water splitting, Journal of Materials Chemistry A, 3 (2015) 156-162, 10.1039/C4TA04863F.
[35] W. Wang, J. Wang, Z. Wang, X. Wei, L. Liu, Q. Ren, W. Gao, Y. Liang, H. Shi, p–n junction CuO/BiVO 4 heterogeneous nanostructures: synthesis and highly efficient visible-light photocatalytic performance, Dalton Transactions, 43 (2014) 6735-6743, 10.1039/C3DT53613K.
[36] C. Sirtori, A. Agüera, W. Gernjak, S. Malato, Effect of water-matrix composition on Trimethoprim solar photodegradation kinetics and pathways, Water research, 44 (2010) 2735-2744, 10.1016/j.watres.2010.02.006.
[37] A. Murata, H. Takada, K. Mutoh, H. Hosoda, A. Harada, N. Nakada, Nationwide monitoring of selected antibiotics: distribution and sources of sulfonamides, trimethoprim, and macrolides in Japanese rivers, Science of the total Environment, 409 (2011) 5305-5312, 10.1016/j.scitotenv.2011.09.014.
[38] A.L. Batt, S. Kim, D.S. Aga, Comparison of the occurrence of antibiotics in four full-scale wastewater treatment plants with varying designs and operations, Chemosphere, 68 (2007) 428-435, https://doi.org/10.1016/j.chemosphere.2007.01.008.
[39] D.W. Kolpin, E.T. Furlong, M.T. Meyer, E.M. Thurman, S.D. Zaugg, L.B. Barber, H.T. Buxton, Pharmaceuticals, hormones, and other organic wastewater contaminants in US streams, 1999− 2000: A national reconnaissance, Environmental science & technology, 36 (2002) 1202-1211, 10.1021/es011055j.
[40] L. Dong, L.L. Yin, Q.N. Xia, X.H. Liu, X.Q. Gong, Y.Q. Wang, Size-dependent catalytic performance of ruthenium nanoparticles in the hydrogenolysis of a beta-O-4 lignin model compound, Catal Sci Technol, 8 (2018) 735-745, 10.1039/c7cy02014g.
[41] J. Bolobajev, M. Kask, K. Kreek, M. Kulp, M. Koel, A. Goi, Metal-doped organic aerogels for photocatalytic degradation of trimethoprim, Chemical Engineering Journal, 357 (2019) 120-128, 10.1016/j.cej.2018.09.127.
[42] K. Chen, D. Xue, Chemoaffinity-mediated crystallization of Cu 2 O: a reaction effect on crystal growth and anode property, CrystEngComm, 15 (2013) 1739-1746, 10.1039/C2CE26500A.
[43] D. Segets, R. Marczak, S. Schäfer, C. Paula, J.-F. Gnichwitz, A. Hirsch, W. Peukert, Experimental and theoretical studies of the colloidal stability of nanoparticles− a general interpretation based on stability maps, ACS nano, 5 (2011) 4658-4669, 10.1021/nn200465b.
[44] K. Chen, S. Song, D. Xue, Chemical reaction controlled synthesis of Cu 2 O hollow octahedra and core–shell structures, CrystEngComm, 15 (2013) 10028-10033, 10.1039/C3CE41745J.
[45] S.D. Pike, E.R. White, A. Regoutz, N. Sammy, D.J. Payne, C.K. Williams, M.S. Shaffer, Reversible Redox Cycling of Well-Defined, Ultrasmall Cu/Cu2O Nanoparticles, ACS Nano, 11 (2017) 2714-2723, 10.1021/acsnano.6b07694.
[46] D.P. Singh, N.R. Neti, A.S.K. Sinha, O.N. Srivastava, Growth of Different Nanostructures of Cu2O (Nanothreads, Nanowires, and Nanocubes) by Simple Electrolysis Based Oxidation of Copper, The Journal of Physical Chemistry C, 111 (2007) 1638-1645, 10.1021/jp0657179.
[47] Y. Wang, N. Herron, NANOMETER-SIZED SEMICONDUCTOR CLUSTERS - MATERIALS SYNTHESIS, QUANTUM SIZE EFFECTS, AND PHOTOPHYSICAL PROPERTIES, Journal of Physical Chemistry, 95 (1991) 525-532, 10.1021/j100155a009.
[48] C.-H. Kuo, M.H. Huang, Facile Synthesis of Cu2O Nanocrystals with Systematic Shape Evolution from Cubic to Octahedral Structures, The Journal of Physical Chemistry C, 112 (2008) 18355-18360, 10.1021/jp8060027.
[49] M. Yin, C.-K. Wu, Y. Lou, C. Burda, J.T. Koberstein, Y. Zhu, S. O'Brien, Copper oxide nanocrystals, Journal of the American Chemical Society, 127 (2005) 9506-9511, 10.1021/ja050006u.
[50] J. Liu, J. Ke, D. Li, H. Sun, P. Liang, X. Duan, W. Tian, M.O. Tadé, S. Liu, S. Wang, Oxygen Vacancies in Shape Controlled Cu2O/Reduced Graphene Oxide/In2O3 Hybrid for Promoted Photocatalytic Water Oxidation and Degradation of Environmental Pollutants, ACS Applied Materials & Interfaces, 9 (2017) 11678-11688, 10.1021/acsami.7b01605.
[51] W. Zou, L. Zhang, L. Liu, X. Wang, J. Sun, S. Wu, Y. Deng, C. Tang, F. Gao, L. Dong, Engineering the Cu2O–reduced graphene oxide interface to enhance photocatalytic degradation of organic pollutants under visible light, Applied Catalysis B: Environmental, 181 (2016) 495-503, https://doi.org/10.1016/j.apcatb.2015.08.017.
[52] G. Yang, S. Cheng, C. Li, J. Zhong, C. Ma, Z. Wang, W. Xiang, Investigation of the oxidation states of Cu additive in colored borosilicate glasses by electron energy loss spectroscopy, Journal of Applied Physics, 116 (2014) 223707, 10.1063/1.4903955.
[53] V.R. Palkar, P. Ayyub, S. Chattopadhyay, M. Multani, Size-induced structural transitions in the Cu-O and Ce-O systems, Physical Review B, 53 (1996) 2167-2170, 10.1103/PhysRevB.53.2167.
[54] C.-K. Wu, M. Yin, S. O'Brien, J.T. Koberstein, Quantitative Analysis of Copper Oxide Nanoparticle Composition and Structure by X-ray Photoelectron Spectroscopy, Chemistry of Materials, 18 (2006) 6054-6058, 10.1021/cm061596d.

[55] H. Azimi, S. Kuhri, A. Osvet, G. Matt, L.S. Khanzada, M. Lemmer, N.A. Luechinger, M.I. Larsson, E. Zeira, D.M. Guldi, C.J. Brabec, Effective Ligand Passivation of Cu2O Nanoparticles through Solid-State Treatment with Mercaptopropionic Acid, Journal of the American Chemical Society, 136 (2014) 7233-7236, 10.1021/ja502221r.
[56] M.C. Biesinger, Advanced analysis of copper X-ray photoelectron spectra, Surface and Interface Analysis, 49 (2017) 1325-1334, 10.1002/sia.6239.
[57] M. Singh, D. Jampaiah, A.E. Kandjani, Y.M. Sabri, E. Della Gaspera, P. Reineck, M. Judd, J. Langley, N. Cox, J. van Embden, E.L.H. Mayes, B.C. Gibson, S.K. Bhargava, R. Ramanathan, V. Bansal, Oxygen-deficient photostable Cu2O for enhanced visible light photocatalytic activity, Nanoscale, 10 (2018) 6039-6050, 10.1039/C7NR08388B.
[58] S. Kumar, C.M.A. Parlett, M.A. Isaacs, D.V. Jowett, R.E. Douthwaite, M.C.R. Cockett, A.F. Lee, Facile synthesis of hierarchical Cu2O nanocubes as visible light photocatalysts, Applied Catalysis B: Environmental, 189 (2016) 226-232, https://doi.org/10.1016/j.apcatb.2016.02.038.
[59] J. Li, M. Jiang, H. Zhou, P. Jin, K.M.C. Cheung, P.K. Chu, K.W.K. Yeung, Vanadium Dioxide Nanocoating Induces Tumor Cell Death through Mitochondrial Electron Transport Chain Interruption, Global Challenges, 3 (2019) 1800058, 10.1002/gch2.201800058.
[60] I.J. Drake, K.L. Fujdala, S. Baxamusa, A.T. Bell, T.D. Tilley, Effects of Precursor Composition on the Local Structure of Cu Dispersed on Mesoporous Silica: A Detailed X-ray Absorption Spectroscopy Study, The Journal of Physical Chemistry B, 108 (2004) 18421-18434, 10.1021/jp040255p.
[61] I. Michael, E. Hapeshi, V. Osorio, S. Perez, M. Petrovic, A. Zapata, S. Malato, D. Barceló, D. Fatta-Kassinos, Solar photocatalytic treatment of trimethoprim in four environmental matrices at a pilot scale: Transformation products and ecotoxicity evaluation, Science of The Total Environment, 430 (2012) 167-173, https://doi.org/10.1016/j.scitotenv.2012.05.003.
[62] M. Abellán, J. Giménez, S. Esplugas, Photocatalytic degradation of antibiotics: the case of sulfamethoxazole and trimethoprim, Catalysis Today, 144 (2009) 131-136, 10.1016/j.cattod.2009.01.051.
[63] Q. Cai, J. Hu, Decomposition of sulfamethoxazole and trimethoprim by continuous UVA/LED/TiO2 photocatalysis: Decomposition pathways, residual antibacterial activity and toxicity, Journal of hazardous materials, 323 (2017) 527-536, 10.1016/j.jhazmat.2016.06.006.
[64] S. Oros-Ruiz, R. Zanella, B. Prado, Photocatalytic degradation of trimethoprim by metallic nanoparticles supported on TiO2-P25, Journal of hazardous materials, 263 (2013) 28-35, 10.1016/j.jhazmat.2013.04.010.
[65] M. Samy, M.G. Ibrahim, M.G. Alalm, M. Fujii, S. Ookawara, T. Ohno, Photocatalytic degradation of trimethoprim using S-TiO2 and Ru/WO3/ZrO2 immobilized on reusable fixed plates, Journal of Water Process Engineering, 33 (2020) 101023, 10.1016/j.jwpe.2019.101023.
[66] X. An, K. Li, J. Tang, Cu2O/Reduced Graphene Oxide Composites for the Photocatalytic Conversion of CO2, ChemSusChem, 7 (2014) 1086-1093, 10.1002/cssc.201301194.
[67] B. Giraldo, W. Yeh, N.P. Kobayashi, Formation of single-crystal Cu2O strips in non-single-crystal CuO thin films by continuous-wave laser diode with micro-chevron laser beam ($$\mu$$µ-CLB), Journal of Materials Science, 55 (2020) 14105-14111, 10.1007/s10853-020-05013-7.
[68] J. Zhu, G. Cheng, J. Xiong, W. Li, S. Dou, Recent Advances in Cu-Based Cocatalysts toward Solar-to-Hydrogen Evolution: Categories and Roles, Solar RRL, 3 (2019) 1900256, 10.1002/solr.201900256.
[69] S. Wang, J. Wang, Trimethoprim degradation by Fenton and Fe(II)-activated persulfate processes, Chemosphere, 191 (2018) 97-105, https://doi.org/10.1016/j.chemosphere.2017.10.040.

*Graphical Abstract

Graphical abstract

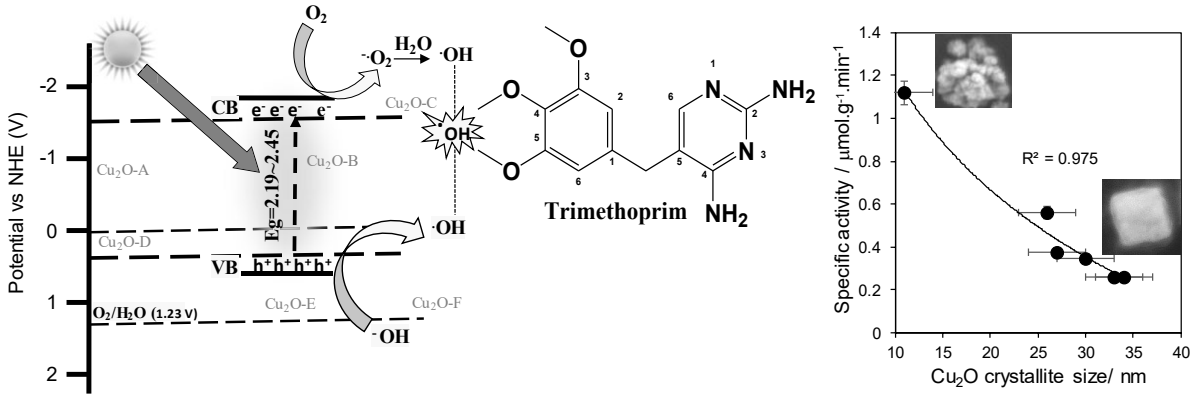

Highlights

- Surfactant- and template-free hydrothermal assembly of hierarchical Cu_2O nanostructures
- Hierarchical Cu_2O active for photocatalytic degradation of the antibiotic trimethoprim under visible light
- Photocatalytic degradation of trimethoprim shows inverse correlation with Cu_2O crystallite size
- Hierarchical Cu_2O photocatalyst exhibits good stability for >25 h

Supplementary Material

Click here to download Supplementary Material: Supporting Information.docx